Electronic Supplementary Information (ESI) for:

Self-Passivation of Low-Dimensional Hybrid Halide Perovskites Guided by Structural Characteristics and Degradation Kinetics

Ke Meng, Xiao Wang, Zhimin Li, Zhou Liu, Zhi Qiao, Chunwu Wang, Youdi Hu, Shunde Li, Lei Cheng, Yufeng Zhai and Gang Chen*

Materials and Methods

Materials. BAI, MAI, PbI_2 and PCBM were bought from Xi'an Polymer Light and all other chemicals were purchased from Sigma-Aldrich. The pure phase n = 2, 3 and 4 species were prepared following the previously reported method.[13]

Preparation of the LDP Film. The LDP film was prepared using the previously reported hot-casting method. Specifically, BAI, PbI_2 and MAI with the molar ratio of 2: 3: 4 were dissolved in the DMSO and DMF mixed solvent (volume ratio of 7: 3) to reach the Pb^{2+} concentration of 1.4 M. The precursor solution was quickly loaded onto the pre-heated substrate which was spun at 5000 rpm for 20 s. The pre-heating temperature for the substrate was set as 80ºC. After spinning, the sample was subsequently annealed at 100 ºC for 10 min to obtain the LDP film.

Preparation of the BAI Treated LDP Film. The BAI treatment was conducted by spin-coating the BAI solution on the LDP film followed by annealing. Typically, 1 mg of BAI was dissolved in 1 mL of isopropanol (IPA) and chlorobenzene mixed solvent (volume ratio of 0.05: 0.95). 50 μL of the BAI solution was spread on the LDP film during spinning at 4000 rpm and the film was further annealed at 100 ºC for 10 min.

Fabrication of Solar Cells. The perovskite solar cells were fabricated featuring a typical p-i-n structure with a fluorine doped tin oxide (FTO) substrate, a NiO hole transport layer (HTL), a LDP or a BAI treated LDP film as light absorber, a PCBM electron transport layer (ETL) and a Au metal electrode. The NiO HTL was prepared by spinning the precursor solution at 2000 rpm for 40 s, which contains 0.1 M nickel acetate tetrahydrate ($Ni(CH_3COO)_2 \cdot 4H_2O$) and 0.1 M ethanolamine ($NH_2CH_2CH_2OH$, EAM) in absolute ethanol. The sample was then annealed at 450 °C for 30 min at the ambient environment. The NiO coated FTO substrate was transferred into the glovebox and

pre-heated to 80 °C. The LDP film was further deposited on the NiO/FTO substrate employing the method described above. The PCBM ETL was prepared by spin-coating the 20 mg/mL PCBM/CB solution at 4000 rpm for 40s. The BCP interlayer was deposited by spin-coating saturated BCP solution in ethanol at 6000 rpm for 20 s. Finally, a 100-nm Au layer was thermally deposited onto ETL to complete the device fabrication.

In Situ GI-XRD Characterization. The synchrotron based GI-XRD measurements were conducted at the beamline BL14B1 of Shanghai Synchrotron Radiation Facility (SSRF). The incident photon energy was 10 keV (wavelength of 1.2398 Å). The diffracted X-rays were collected using the 2D Mar225 CCD detector. The cell for the in situ GI-XRD measurement was specially designed which contained a Kapton window allowing the transmission of X-rays, a gas-circulating system to provide and maintain the inert or humidity atmosphere and a programmable heating stage. The collection interval in the in situ experiments was set as 10 s. The 2D GI-XRD data were converted to the 1D curves using the Fit2D software. The background was removed using the cubic spline fitting.

Other Characterizations. A field emission scanning electron microscopy (FESEM, 7800F Prime, JEOL Japan) was employed for the morphological characterization of the films. A UV-Vis-NIR spectrometer (Agilent Cary 5000) equipped with an integrating sphere was used to obtain the absorption and reflectance spectra. The photoluminescence (PL) spectra were recorded with a Fluorescence Spectrometer (Horiba FL-3) where a 350 nm excitation wavelength and a 510 nm high pass optical filter were employed. The TG-MS experiments were conducted using a PerkinElmer TG-MS system. The LDP powders were scraped and collected for the TG-MS measurement. The X-ray diffraction data for the film stability studies were obtained using the D8 Advance (Bruker) instrument. The photocurrent density–voltage (*J–V*) curves of solar cells were measured using a Keithley 2400 source meter under the illumination of a solar simulator (SS-F5-3A/SS-F7-3A, Enlitech. Co. Ltd. Taiwan, China). An NREL-certified Si solar cell with a KG-5 filter was employed to acquire a 100 mW/cm^2 (AM 1.5G) light intensity. The reverse scan (the direction from open circuit to 0 V) and a step voltage of 30 mV were used for the *J-V* measurements. An aperture area of 0.059 cm^2 was defined by a non-reflective metallic shadow mask.

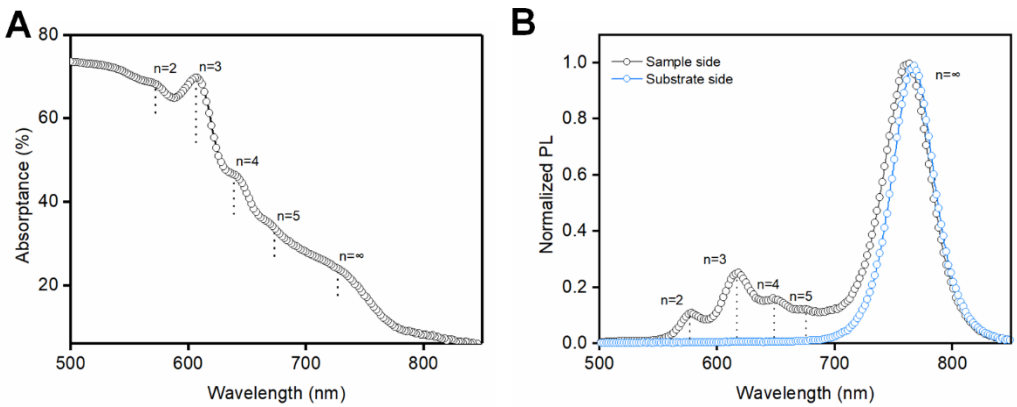

Figure S1. (a) UV-vis absorption and (b) PL spectra of the LDP film. In (a), the UV-vis absorption spectrum contains the absorption features corresponding to the n = 2, 3, 4 …, ∞ species, which reveals the multi-phase nature of the LDP film. In (b), a single PL peak is shown at ca. 765 nm when illuminating from the sample side, indicating that the surface of the LDP film consists mainly the 3D-like species. The PL peaks associated with the n = 2-5 and the n = ∞ perovskites are separately observed at 575, 615, 645, 675 and 760 nm when illuminating from the substrate side. The PL results reveal the phase separation in the LDP film.

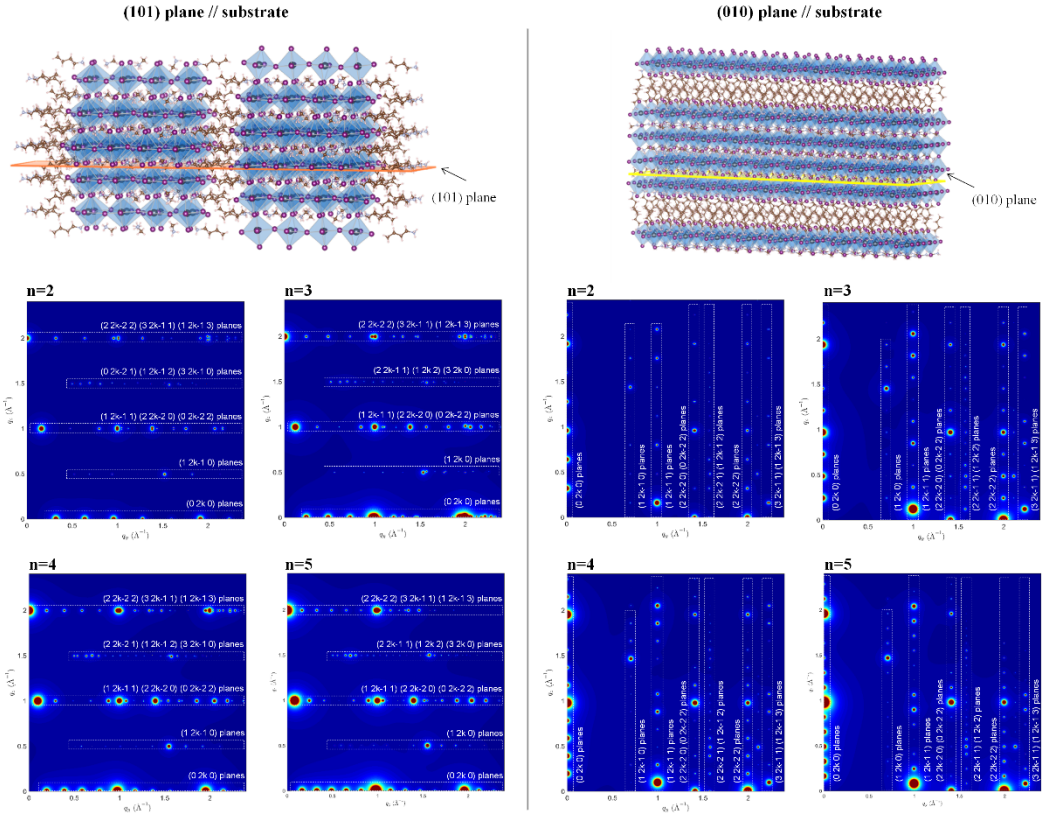

Figure S2. Simulated 2D XRD patterns of the n = 2-5 perovskite species at the schematically illustrated orientations. Considering the mixed-phase nature of the LDP film, the 2D XRD patterns of the different 2D perovskites (n = 2-5; where n represents the thickness of the Pb-I slabs) at specific orientations are simulated and presented in this figure (the diffraction spots are separately labelled with the corresponding crystal planes, where k = 1, 2, 3…). The results confirm the vertical alignment of the 2D perovskite species in the LDP film with the (101) plane parallel to the substrate.

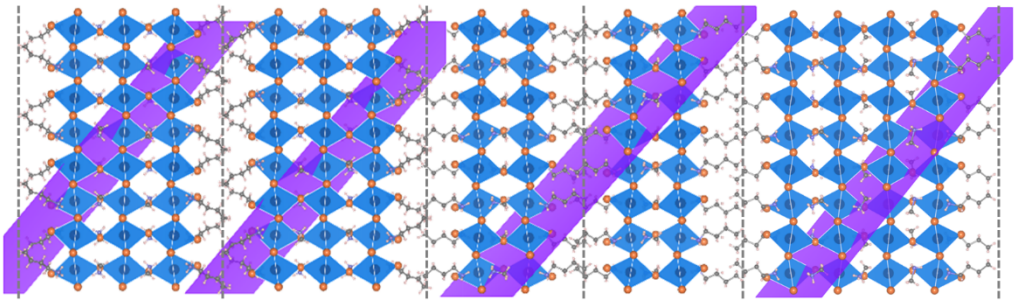

Figure S3. Schematic illustration for the missing of the (0k0) diffraction signal and the origin of the (1 2n+1 1) diffraction signals. The scheme depicts the distribution of the Pb-I slab thicknesses along the direction parallel to the substrate. The insufficient coherency of the crystals leads to the missing of the diffraction signal from the (0k0) planes (dashed lines). The purple slabs represent the (1 2n+1 1) crystal planes for the species with various n values, namely (151) plane for n = 2, (171) plane for n = 3, (191) plane for n = 4 and (1 11 1) plane for n = 5. The d-spacing for the (1 2n+1 1) planes for the n = 2-5 species are 4.91, 4.80, 4.73 and 4.69 Å, respectively. It is ascertained that the (1 2n+1 1) diffraction peak in **Figure 1f** is ascribed to the n = 2-5 species.

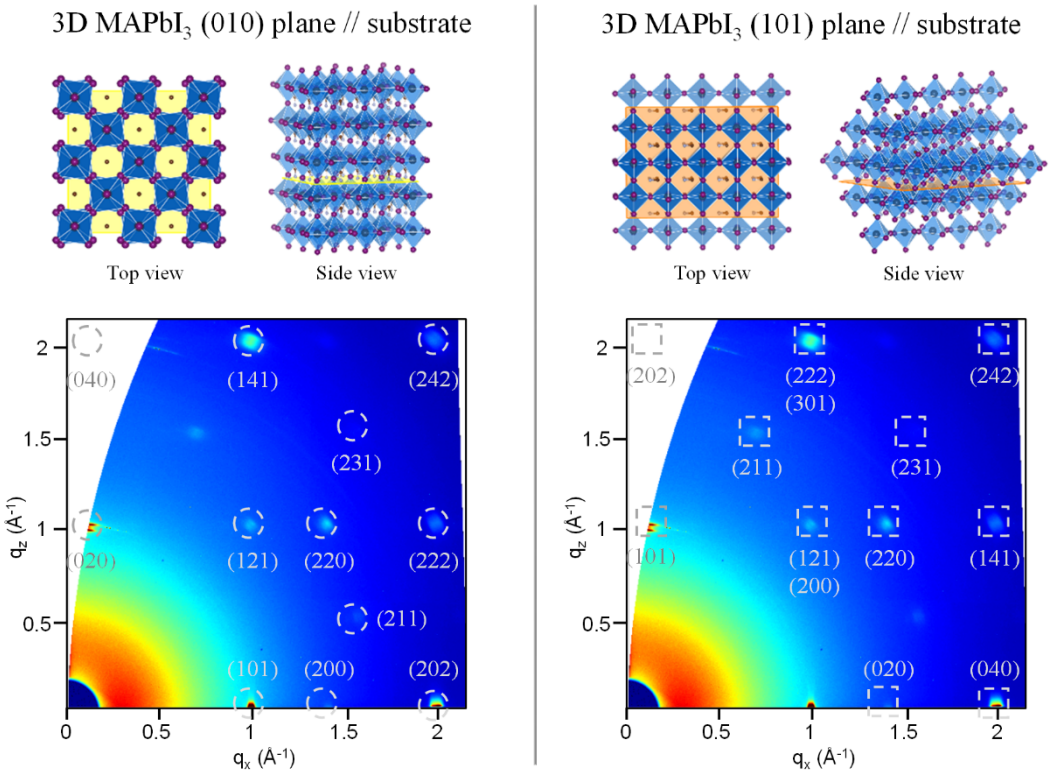

Figure S4. The simulated diffraction signals of $MAPbI_3$ at the schematically illustrated orientations. The simulated Bragg spots of the 3D $MAPbI_3$ perovskite at the orientations with the (010) and (101) planes parallel to the substrate are separately presented (note that tetragonal structure of $MAPbI_3$ with the unit cell dimensions of a = 8.8392 Å, b= 12.6948 Å and c = 8.8392 Å is employed for the simulation). Clearly, the experimental XRD pattern as shown in **Figure 1c** is the superposition of the diffraction signals from both orientations.

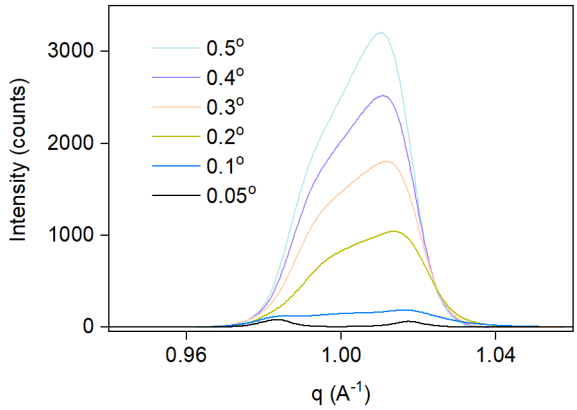

Figure S5. Peak intensity evolution of the diffraction peak at q around 1 Å^{-1} for different incident angles. The 2D GI-XRD patterns of the LDP film at the incident angles from 0.05 to 0.5º are recorded. The targeted Bragg spots are separately integrated and the resultant 1D XRD patterns are presented in this figure. By fitting and deconvoluting the peaks, the peak intensities of the involved species are presented in Table S1.

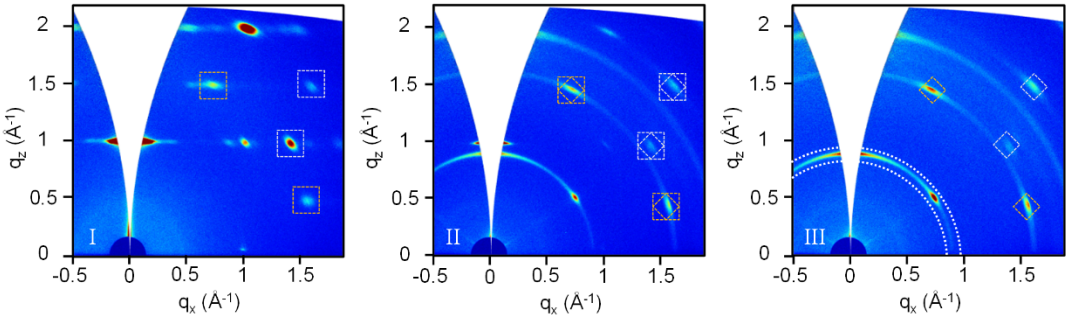

Figure S6. The typical 2D and 1D XRD patterns of the film taken at the points I-III as denoted in Figure 2a.

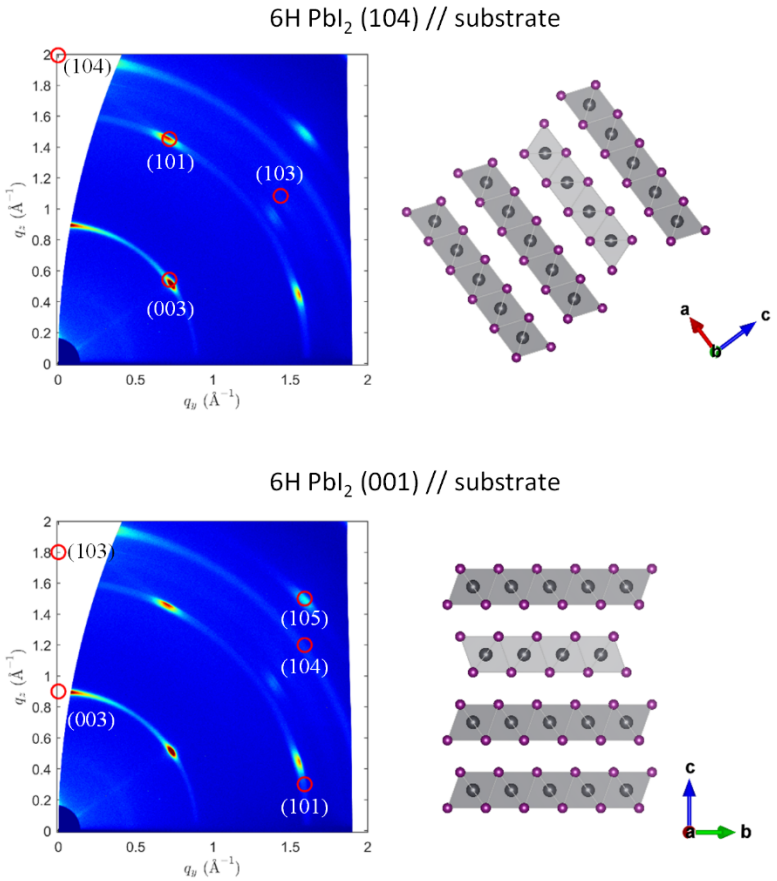

Figure S7. Orientation of the PbI_2 film. The simulated Bragg spots of PbI_2 at the orientations with the (104) and (001) planes parallel to the substrate (denoted by red circles). The diffraction spots in the experimental 2D GI-XRD pattern of the resultant PbI_2 film are originated from both orientations.

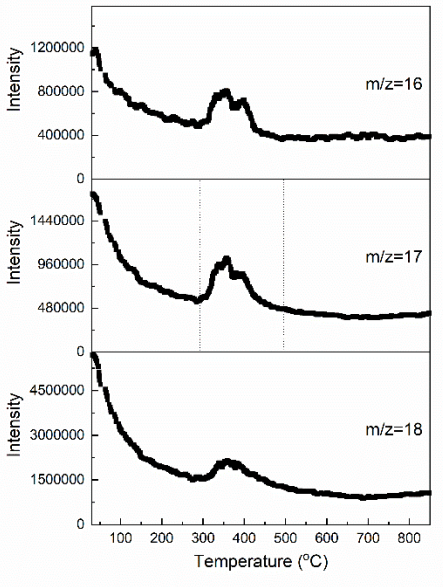

Figure S8. Intensity vs. temperature plots for the selected m/z peaks recorded simultaneously in the MS analyses during the thermal degradation process (heating rate of 10 °C/min) of the LDP powders. The m/z peaks at 16, 17 and 18 could be assigned to the NH_2^+, NH_3^+ and NH_4^+ ions originating from the parent molecule and the fragment of NH_3.

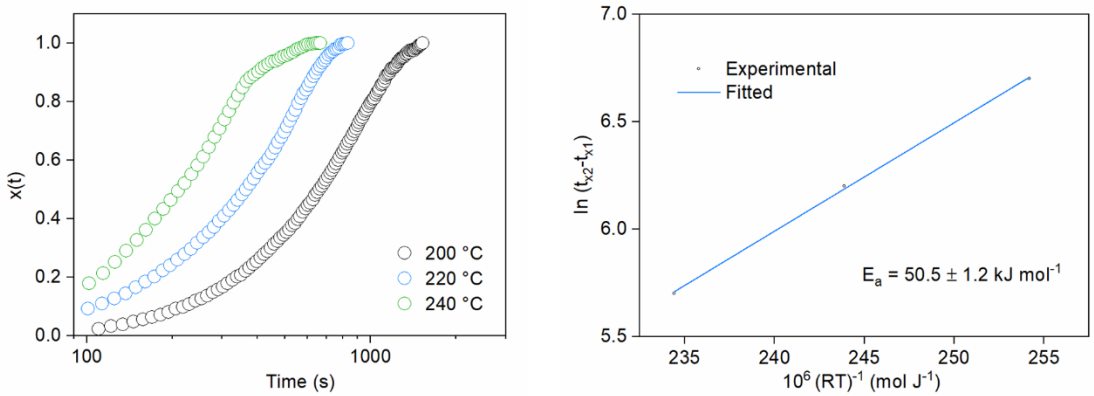

Figure S9. Activation energy for the thermal degradation of the $MAPbI_3$ film. The 3D perovskite films are prepared employing the typical solvent-engineering method, followed by the isothermal aging at the temperature of 200, 220 and 240 ºC respectively. The activation energy of E_a is estimated to be 50.5 ± 1.2 kJ mol^{-1} for the degradation of $MAPbI_3$.

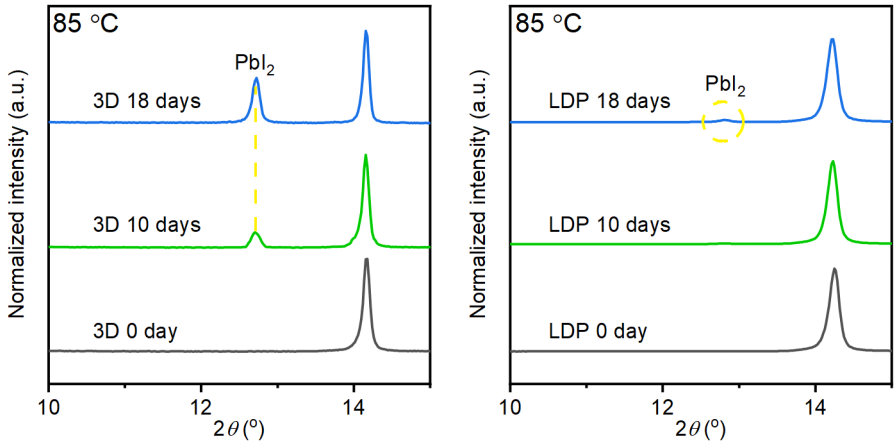

Figure S10. XRD pattern evolutions of the 3D $MAPbI_3$ and LDP films aging at 85 ºC.

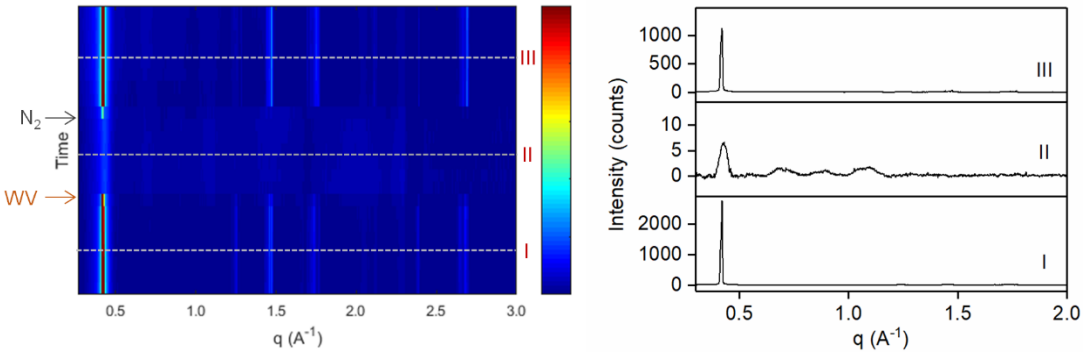

Figure S11. 2D intensity colour mapping following the transformation process of the BAI film through one WVAR cycle. The BAI film (obtained by spin-coating the BAI/IPA solution on glass substrate) was exposed to one WVAR cycle. The typical XRD patterns of the as-prepared BAI film (I), the hydrated BAI film (II) and the dried BAI film (III) are separately presented in the right panel. Note that both BAI and its hydrate species exhibit diffraction peaks at 0.42 $Å^{-1}$.

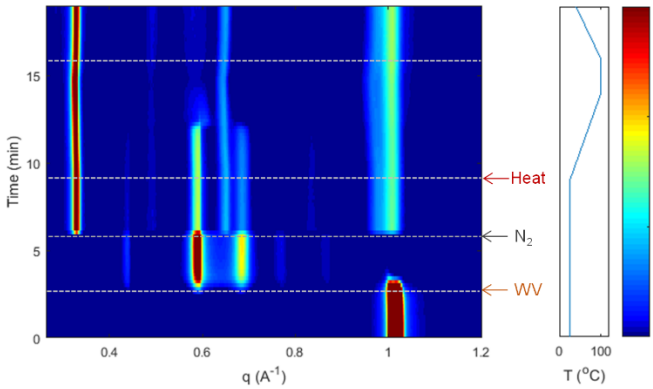

Figure S12. 2D intensity colour mapping following the transformation process of the LDP film through one WVAR cycle followed by the annealing/cooling process (blue line shows the temperature ramping profile). At RT in dry condition, the transformation from the 2D intermediate to the perovskite phase is a partial reaction, which is indicated by the presence of the diffraction signals from the hydrated species. The 2D intermediate film fully transforms into the perovskite phase after the annealing process.

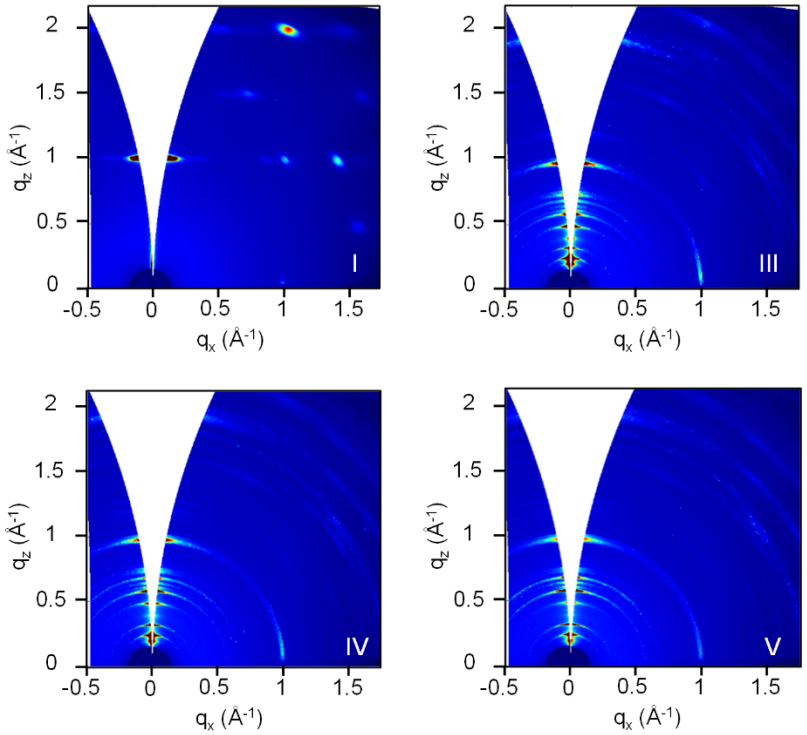

Figure S13. 2D GI-XRD patterns of the LDP film at the points of I, III, IV and V in Figure 4a. The film exhibits the (0 k 0) diffraction rings and intense Bragg spots on the q_z axes, indicating that the regenerated perovskite species exhibit a random orientation with crystals predominantly aligned parallel to the substrate.

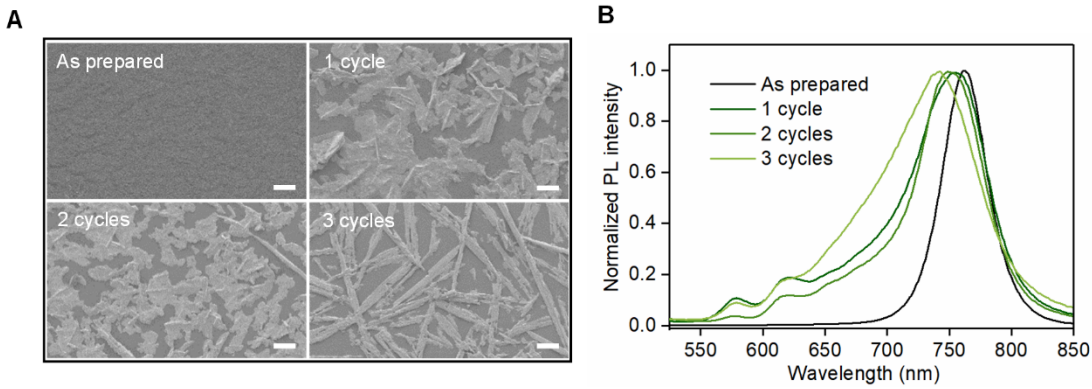

Figure S14. (a) SEM images and (b) PL spectra of the samples at the points of I, III, IV and V in Figure 4a (the scale bars in the SEM images are 10 μm).

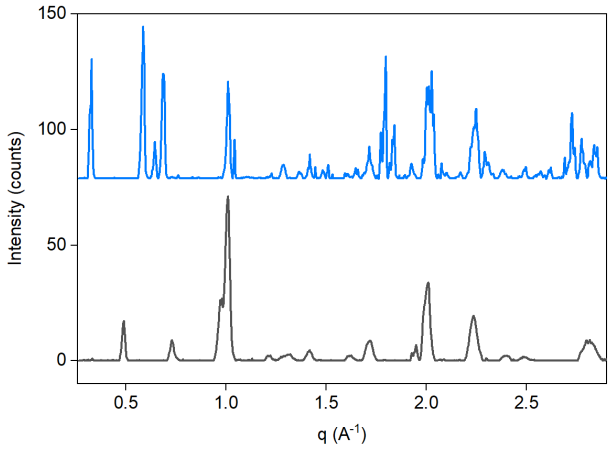

Figure S15. XRD patterns of the n = 3 species before and after the WVAR treatment. The as-prepared n = 3 species shows the diffraction peaks at q of 0.49 and 0.73 $Å^{-1}$. After the WVAR treatment, the new diffraction peaks at q of 0.33 and 0.64 $Å^{-1}$ emerge, indicating that it is transformed into the n = 2 species.

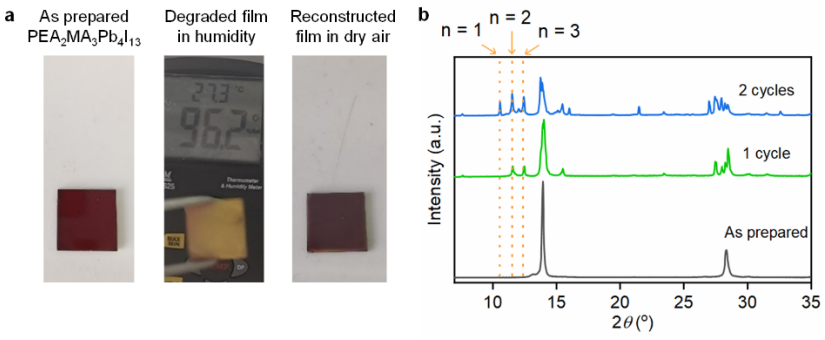

Figure S16. The degradation and reconstruction of the $(PEA)_2(MA)_3Pb_4I_{13}$ LDP film. (a) Digital photos of the $(PEA)_2(MA)_3Pb_4I_{13}$ LDP film taken at various conditions. (b) XRD pattern evolution of the $(PEA)_2(MA)_3Pb_4I_{13}$ LDP film for two WVAR cycles.

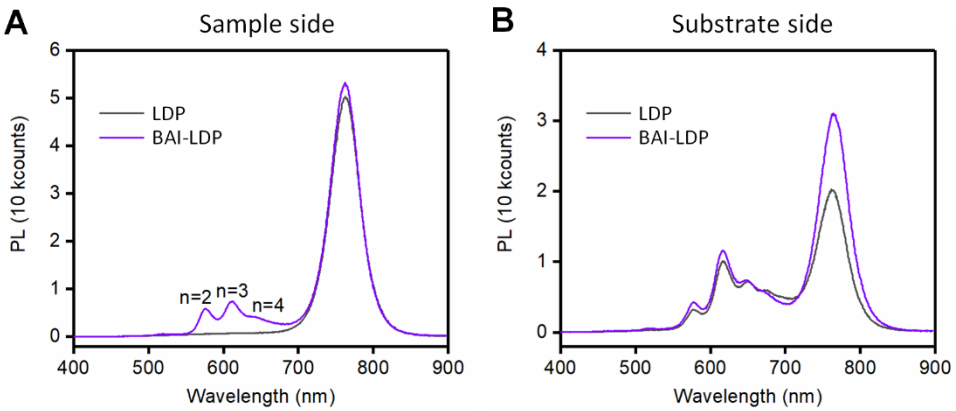

Figure 17. PL spectra of the LDP and BAI-LDP films. Figure S17a presents the PL spectra of the films illuminated from the sample side. The emergence of the PL peaks at 575, 615 and 645 nm after the PL treatment indicates the formation of n = 2-4 species at the surface of the LDP film. The missing of the XRD signals of the n=3 and 4 species could be attributed to the insufficient coherency of crystals. **Figure S17b** presents the PL spectra of the films illuminated from the substrate side. The nearly identical spectra indicate that the transformation reaction only occurs at the surface of the LDP film.

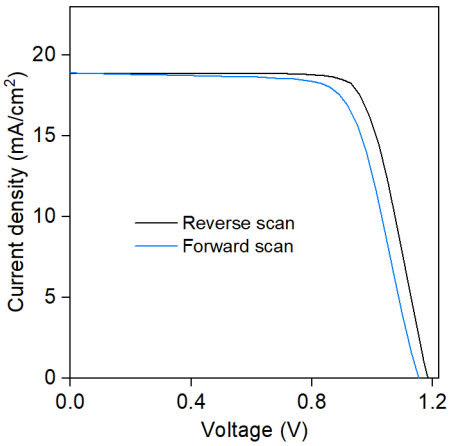

Figure S18. The reverse and forward *J-V* scans of the device based on the BAI-LDP film.

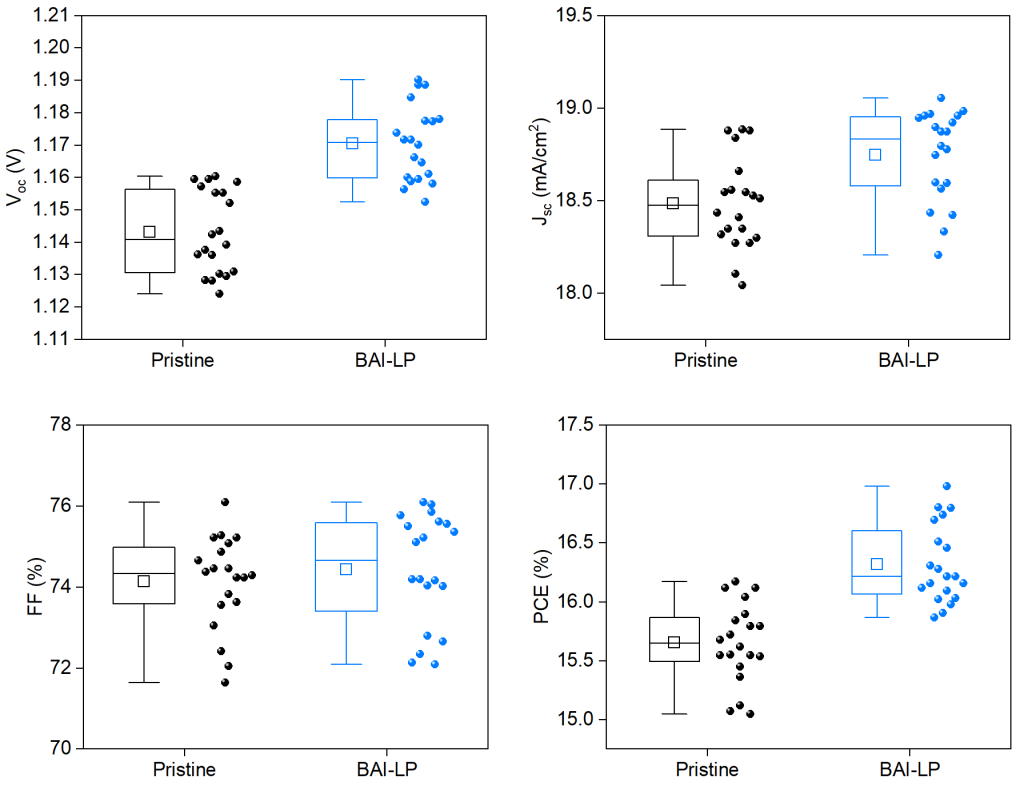

Figure S19. Statistical photovoltaic parameters of the PSCs based on the LDP and BAI-LDP film. The statistical photovoltaic parameters are collected based on 20 cells for each condition. The upper and lower error bars represent the maximum and minimum values respectively. The square and mid-line in each box represent the mean and median value, respectively. The top and the bottom of the box represent the upper and lower quartile.

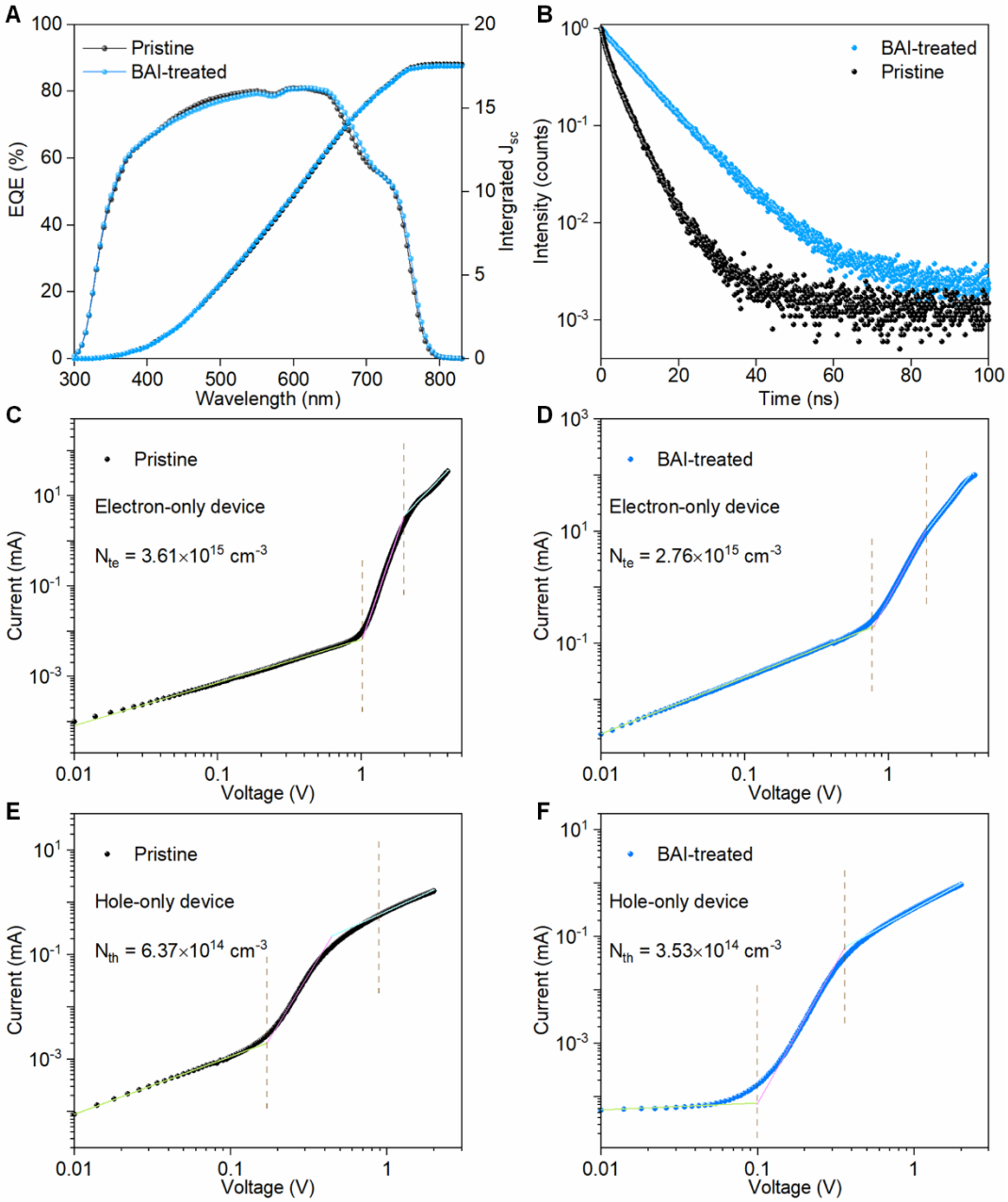

Figure S20. Charge carrier transport behaviours in the LDP and BAI-LDP based devices. (**a**) The external quantum efficiency (EQE) spectra of the LDP and BAI-LDP based devices, respectively. The integrated J_{sc} for the two devices show identical values, which is in accordance with the *J-V* results. (**b**) The time-resolved photoluminescence spectra of the LDP and BAI-LDP films. The results show that the BAI-LDP film possesses the elongated PL lifetime, indicating there are less defect states. (**c** to **f**) Space-charge-limited current experiment results of the electron/hole-only devices. The results suggest that the BAI-LDP film possesses lower defect densities due to the passivation effect. The electron-only device features a structure of FTO/ SnO_2 /LDP or BAI-LDP/ PCBM/ Ag and the hole-only device contains the components of FTO/ NiO /LDP or BAI-LDP/ Spiro-OMeTAD/ Ag.

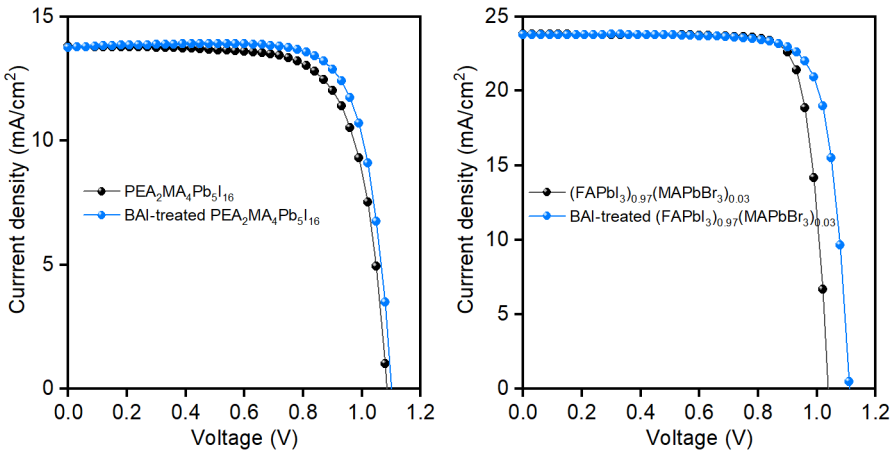

Figure S21. *J-V* characteristics of the typical PSC devices based on the $(PEA)_2(MA)_4Pb_5I_{16}$ LDP and 3D $(FAPbI_3)_{0.97}(MAPbBr_3)_{0.03}$ films with and without the BAI treatment.

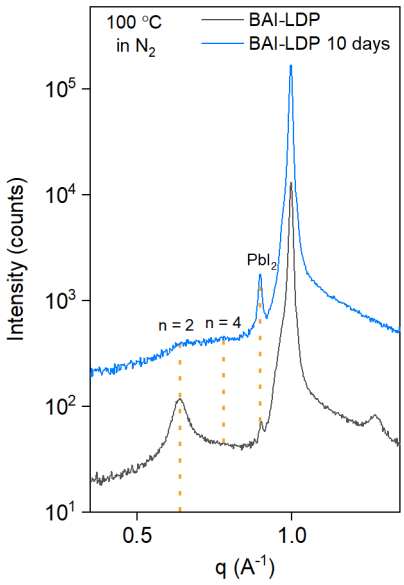

Figure S22. Zoomed-in XRD patterns of the BAI-LDP film before and after thermal aging at 100 °C for 10 days (Intensity is plotted in the logarithmic scale).

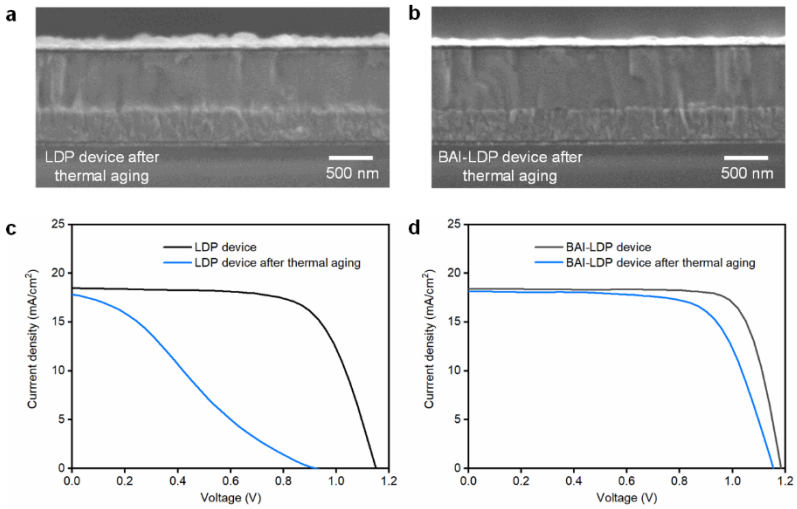

Figure S23. Characterizations of the devices after thermal aging. The cross-sectional SEM image of (a) the LDP-based device and (b) the BAI-LDP based device after thermal aging. The typical *J-V* characteristics of (c) the LDP-based device and (d) the BAI-LDP based device taken before and after thermal aging.

Table S1. The fitted areal intensities of the diffraction peaks corresponding to each species at the specific incident angles as shown in Figure S5.

Species/ peak area	**0.05°**	**0.1°**	**0.2°**	**0.3°**	**0.4°**	**0.5°**
3DS	79	114	N/A			
2D	NA	74	795	1355	1763	2111
3DB	61	180	725	1386	2107	2720